

Schwarz-preconditioned HMC algorithm for two-flavour lattice QCD

Martin Lüscher

*CERN, Physics Department, TH Division
CH-1211 Geneva 23, Switzerland*

Abstract

The combination of a non-overlapping Schwarz preconditioner and the Hybrid Monte Carlo (HMC) algorithm is shown to yield an efficient simulation algorithm for two-flavour lattice QCD with Wilson quarks. Extensive tests are performed, on lattices of size up to 32×24^3 , with lattice spacings $a \simeq 0.08$ fm and at bare current-quark masses as low as 21 MeV.

1. Introduction

At present, perhaps the greatest obstacle in lattice QCD is the fact that the efficiency of the established simulation algorithms rapidly decreases when the continuum limit is approached and the masses of the light quarks are scaled towards their physical values [1–11]. The dynamics of these algorithms is still not fully understood, but it is quite clear that the poor scaling behaviour is driven by the condition number of the lattice Dirac operator, which grows inversely proportionally to the lattice spacing and the quark mass.

Preconditioning is usually perceived as a technique for the efficient solution of ill-conditioned systems of linear equations [12]. This kind of preconditioning is routinely applied in lattice QCD to accelerate the solver for the lattice Dirac equation. While the solver is a central element of the HMC simulation algorithm [13], it is also possible to precondition this algorithm itself, using another preconditioner perhaps, by factorizing the quark determinant into the determinants of the preconditioners and the preconditioned Dirac operator. The magnitude of the quark force terms in

the molecular dynamics equations is then often reduced, which allows the associated integration step sizes to be set to larger values and thus leads to an acceleration of the algorithm [14–18,10].

In the present paper the effectiveness of a non-overlapping Schwarz preconditioner for the HMC algorithm is studied. The application of the Schwarz alternating procedure in lattice QCD has previously been advocated in refs. [19,20], and some familiarity with the second of these papers will be assumed here. In order to bring out the underlying strategies more clearly, the general structure of the preconditioned HMC algorithm is first discussed. The Schwarz-preconditioned algorithm is then introduced in sect. 3 and the results of some test runs are reported in sect. 4.

2. Preconditioned HMC algorithm

Only the standard Wilson formulation [21] of lattice QCD will be considered in this paper, with bare coupling g_0 and bare quark mass m_0 , but the algorithm is set up in such a way that $O(a)$ improvement [22,23] and more complicated gauge actions with double-plaquette terms [24,25] can be easily included. As usual a four-dimensional hypercubic lattice of size $T \times L^3$ will be assumed, with lattice spacing a set to unity for convenience, and periodic boundary conditions in all directions, except for the quark fields, which are taken to be antiperiodic in time. Any unexplained notations are as in ref. [20].

2.1 Factorization of the quark determinant

In the familiar case of even–odd preconditioning, the lattice points are ordered such that the even ones come first and the (massive) Wilson–Dirac operator $D \equiv D_w + m_0$ then assumes the block form

$$D = \begin{pmatrix} A_{11} & A_{12} \\ A_{21} & A_{22} \end{pmatrix} \tag{2.1}$$

in position space. Whenever the Dirac operator is written in this way, its determinant may be factorized according to

$$\det D = \det A_{11} \det A_{22} \det \{ 1 - A_{11}^{-1} A_{12} A_{22}^{-1} A_{21} \}, \tag{2.2}$$

where the operator in the curly bracket is referred to as the preconditioned Dirac

operator or (in the mathematical literature) as the *Schur complement* of the Dirac operator with respect to the block decomposition (2.1).

In general, preconditioning is always associated with a factorization

$$\det D = \det R_1 \dots \det R_n \quad (2.3)$$

of the quark determinant into the determinants of certain operators R_k . How many factors one obtains, and in exactly which spaces of fields the operators act, depends on the chosen preconditioner. It is also possible to combine several preconditioners, which may result in further factorizations. Just to mention an example, the simple polynomial preconditioning of the even–odd preconditioned Wilson–Dirac operator \hat{D} , which was recently considered in refs. [16–18], leads to

$$R_1 = \hat{D} + M, \quad R_2 = \hat{D}(\hat{D} + M)^{-1}, \quad (2.4)$$

where M is an adjustable mass parameter.

2.2 Preconditioned molecular dynamics

For any given factorization of the quark determinant, the HMC algorithm for two-flavour QCD can be set up in the standard manner. First the link momenta $\Pi(x, \mu)$ and the appropriate pseudo-fermion fields $\phi_1(x), \dots, \phi_n(x)$ (one for each factor of the determinant) need to be introduced. These fields are elements of certain linear spaces that are assumed to be equipped with the obvious scalar products. The HMC hamiltonian may then be written in the compact form

$$H = \frac{1}{2} (\Pi, \Pi) + S_G + \sum_{k=1}^n (R_k^{-1} \phi_k, R_k^{-1} \phi_k), \quad (2.5)$$

where S_G denotes the action of the gauge field.

Starting from this expression, the forces in the molecular dynamics equations

$$\frac{d}{d\tau} \Pi(x, \mu) = - \sum_{k=0}^n F_k(x, \mu), \quad (2.6)$$

$$\frac{d}{d\tau} U(x, \mu) = \Pi(x, \mu) U(x, \mu), \quad (2.7)$$

are obtained by differentiation with respect to the link variables. They take values in the Lie algebra of $SU(3)$ and are such that

$$(\omega, F_0) = \delta_\omega S_G, \quad (2.8)$$

$$(\omega, F_k) = 2\text{Re}(R_k^{-1}\phi_k, \delta_\omega R_k^{-1}\phi_k), \quad k = 1, \dots, n, \quad (2.9)$$

for all infinitesimal variations

$$\delta_\omega U(x, \mu) = \omega(x, \mu)U(x, \mu) \quad (2.10)$$

of the gauge field.

Among the operators R_k there is normally one, say R_n , which is the preconditioned Wilson–Dirac operator or a closely related operator. In the course of the numerical integration of the molecular dynamics equations, the linear equation

$$R_n\psi = \eta \quad (2.11)$$

must be solved many times and this part of the calculation is then likely to consume most of the computer time, particularly at small quark masses. An important point to note here is that the solution of eq. (2.11) can be obtained by solving the equivalent Wilson–Dirac equation, using a preconditioner and a solver that are optimal for this task. In the case of the factorization (2.2), for example, there are $n = 3$ operators,

$$R_1 = A_{11}, \quad R_2 = A_{22}, \quad R_3 = 1 - A_{11}^{-1}A_{12}A_{22}^{-1}A_{21}, \quad (2.12)$$

and eq. (2.11) is equivalent to

$$D\chi = \begin{pmatrix} A_{11}\eta \\ 0 \end{pmatrix}, \quad \chi = \begin{pmatrix} \psi \\ * \end{pmatrix}. \quad (2.13)$$

The preconditioner used for the solution of this equation and the one that determines the factorization of the quark determinant thus do not need to be the same. These two kinds of preconditioning should be kept separate and must actually satisfy quite different criteria, as will become clear below.

2.3 Multiple step size integration

The widely used numerical integration schemes for the molecular dynamics equations can be considered to be sequences of elementary steps in which either all momenta $\Pi(x, \mu)$ or all link variables $U(x, \mu)$ are updated. For a step of size ϵ , these elementary operations are

$$\mathfrak{T}_k(\epsilon) : \quad \Pi(x, \mu) \rightarrow \Pi(x, \mu) - \epsilon F_k(x, \mu), \quad k = 0, \dots, n, \quad (2.14)$$

$$\mathfrak{T}_U(\epsilon) : \quad U(x, \mu) \rightarrow \text{E}(\epsilon\Pi(x, \mu))U(x, \mu), \quad (2.15)$$

where $E(X)$ stands for the $SU(3)$ exponential function or some suitable approximation to it (see appendix A). The leap-frog integration from molecular dynamics time 0 to τ , for example, amounts to the application of the product

$$\left\{ \mathfrak{T}_0(\frac{1}{2}\epsilon) \dots \mathfrak{T}_n(\frac{1}{2}\epsilon) \mathfrak{T}_U(\epsilon) \mathfrak{T}_0(\frac{1}{2}\epsilon) \dots \mathfrak{T}_n(\frac{1}{2}\epsilon) \right\}^N, \quad \epsilon = \frac{\tau}{N}, \quad (2.16)$$

to the initial field configuration. As is well known, this popular integrator converges with a rate proportional to ϵ^2 and satisfies the basic theoretical requirements, i.e. it preserves the measure in phase space and is exactly time-reversible.

If the forces F_0, \dots, F_n have sizeably different magnitudes such that, say, $\|F_0\|$ is larger than $\|F_1\|$, which is larger than $\|F_2\|$, and so on, it is possible to accelerate the integration by adopting a hierarchical scheme [26,27]. First an integrator

$$\mathfrak{J}_0(\tau, N_0) = \left\{ \mathfrak{T}_0(\frac{1}{2}\epsilon) \mathfrak{T}_U(\epsilon) \mathfrak{T}_0(\frac{1}{2}\epsilon) \right\}^{N_0}, \quad \epsilon = \frac{\tau}{N_0}, \quad (2.17)$$

is defined, which neglects all quark forces F_1, \dots, F_n . More complicated integrators that include an increasing number of these forces are then constructed recursively through

$$\begin{aligned} \mathfrak{J}_k(\tau, N_0, \dots, N_k) = \\ \left\{ \mathfrak{T}_k(\frac{1}{2}\epsilon) \mathfrak{J}_{k-1}(\epsilon, N_0, \dots, N_{k-1}) \mathfrak{T}_k(\frac{1}{2}\epsilon) \right\}^{N_k}, \quad \epsilon = \frac{\tau}{N_k}. \end{aligned} \quad (2.18)$$

The full integrator $\mathfrak{J}_n(\tau, N_0, \dots, N_n)$ that is obtained in this way is characterized by the time intervals

$$\epsilon_k = \frac{\tau}{N_k N_{k+1} \dots N_n} \quad (2.19)$$

at which the forces F_k need to be evaluated.

In practice the step numbers N_k must be such that the shifts $\epsilon_0 \Pi$ and $\epsilon_k F_k$ remain small along the molecular dynamics trajectory. The smaller the forces are the larger the step sizes can be, and whether a reduction of the computational effort is achieved thus depends on the magnitudes of the forces and the difficulty to compute them.

2.4 Choosing a preconditioner

In general the preconditioning of the HMC algorithm is beneficial because it leads to smaller quark forces along the molecular dynamics trajectories. Ideally the preconditioning should be such that the forces that are relatively expensive to calculate (in terms of the required computer time) are those with the smallest magnitude.

Preconditioning may also soften the scaling behaviour of the simulation algorithm with respect to the quark mass. When the chiral limit is approached, the quark forces tend to increase, and probably become more irregular too, which requires the step sizes to be adjusted accordingly. In a recent study of two-flavour QCD at small quark masses by Namekawa et al. [11], for example, the step sizes had to be decreased roughly in proportion to the quark mass. The choice of the preconditioner can have an influence on this behaviour, as will be shown later in this paper.

Eventually the performance of the preconditioned algorithm must be determined empirically, since the dependence of the autocorrelation times of the quantities of interest on the preconditioner is difficult to foresee. The suitability of the algorithm for parallel processing and other practical issues may also have to be taken into account at this point.

3. Schwarz-preconditioned algorithm

The classical Schwarz alternating procedure was previously considered as a preconditioner for the Wilson–Dirac equation [20]. When combined with the generalized conjugate residual (GCR) algorithm, this preconditioner proved to be very efficient, and it will now be used, in its simplest form with cycle number $n_{cy} = 1$, to precondition the HMC algorithm.

3.1 Domain decomposition

Following ref. [20] the lattice is covered by a regular grid of non-overlapping rectangular blocks Λ . For technical reasons the block sizes are assumed to be even and to be such that the blocks can be chessboard-coloured, i.e. that there is an even number of blocks in all dimensions. The union of the black blocks is then denoted by Ω and the union of the white blocks by Ω^* (see fig. 1).

With respect to an ordering of the lattice points where those in Ω come first, the Wilson–Dirac operator assumes the block form

$$D = \begin{pmatrix} D_{\Omega} & D_{\partial\Omega} \\ D_{\partial\Omega^*} & D_{\Omega^*} \end{pmatrix}. \quad (3.1)$$

The operator D_{Ω} , for example, coincides with the Wilson–Dirac operator on Ω with Dirichlet boundary conditions, while $D_{\partial\Omega}$ is the sum of all hopping terms from the exterior boundary $\partial\Omega$ of Ω to the boundary $\partial\Omega^*$ of Ω^* .

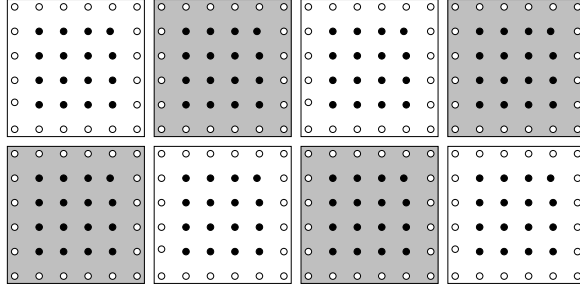


Fig. 1. Two-dimensional cross-section of a 24×12^3 lattice covered by non-overlapping 6^4 blocks Λ . The domains Ω and Ω^* are the unions of the black and white blocks respectively, and their exterior boundaries $\partial\Omega$ and $\partial\Omega^*$ consist of all points in the complementary domain represented by open circles.

It is often convenient to let these operators act on quark fields that are defined on the whole lattice rather than on Ω or Ω^* only. The extension is done in the obvious way by padding with zeros so that eq. (3.1), for example, may be written as

$$D = D_\Omega + D_{\Omega^*} + D_{\partial\Omega} + D_{\partial\Omega^*}. \quad (3.2)$$

Similarly the further decompositions into block operators read

$$D_\Omega + D_{\Omega^*} = \sum_{\text{all } \Lambda} D_\Lambda, \quad (3.3)$$

$$D_{\partial\Omega} = \sum_{\text{black } \Lambda} D_{\partial\Lambda}, \quad D_{\partial\Omega^*} = \sum_{\text{white } \Lambda} D_{\partial\Lambda}, \quad (3.4)$$

where D_Λ denotes the Wilson–Dirac operator on the block Λ with Dirichlet boundary conditions and $D_{\partial\Lambda}$ the sum of the hopping terms that move the field components on the exterior boundary $\partial\Lambda$ of the block Λ to its interior boundary points.

3.2 Quark determinant

The factorization

$$\det D = \det D_\Omega \det D_{\Omega^*} \det \left\{ 1 - D_\Omega^{-1} D_{\partial\Omega} D_{\Omega^*}^{-1} D_{\partial\Omega^*} \right\} \quad (3.5)$$

is now deduced from the block structure (3.1) as in the case of the even–odd preconditioning considered in subsect. 2.1. However, contrary to what might be suspected, the operator in the curly bracket is not quite the same as the Schwarz-preconditioned

Wilson–Dirac operator of ref. [20], with cycle number $n_{cy} = 1$, but their determinants coincide and the factorization (3.2) may therefore be regarded as the one that is naturally associated to the Schwarz preconditioner.

Some further reductions and factorizations of the quark determinant are still possible at this point. The decomposition (3.3), for example, leads to the identity

$$\det D_\Omega \det D_{\Omega^*} = \prod_{\text{all } \Lambda} \det \hat{D}_\Lambda, \quad (3.6)$$

in which \hat{D}_Λ stands for the even–odd preconditioned Wilson–Dirac operator on the block Λ with Dirichlet boundary conditions. Another observation is that the operator in the curly bracket in eq. (3.5) (the Schur complement) acts non-trivially on only those components of the quark fields that reside on $\partial\Omega^*$. Its determinant can therefore be reduced to the space of all fields supported on this subset of points. As explained in appendix B, a reduction to an even smaller subspace $V_{\partial\Omega^*}$ of fields is in fact possible when the detailed properties of $D_{\partial\Omega^*}$ are taken into account.

Contact with the general form of the preconditioned HMC algorithm discussed in the previous section is now made by setting $n = 2$ and

$$R_1 = \sum_{\text{all } \Lambda} \hat{D}_\Lambda, \quad (3.7)$$

$$R_2 = 1 - P_{\partial\Omega^*} D_\Omega^{-1} D_{\partial\Omega} D_{\Omega^*}^{-1} D_{\partial\Omega^*}, \quad (3.8)$$

where $P_{\partial\Omega^*}$ denotes the orthonormal projector to the subspace $V_{\partial\Omega^*}$ (appendix B). In particular, R_2 is considered to be an operator in this space, while R_1 operates on quark fields that are defined on the even points of the full lattice.

3.3 Block decoupling

The classical Schwarz procedure obtains the solution of the Wilson–Dirac equation in an iterative process, where all black and all white blocks are visited alternately and the equation is solved there with Dirichlet boundary values given by the current approximation to the solution [20]. Since the lattice Dirac operator involves only nearest-neighbour hopping terms, the equations on the black blocks (and similarly those on the white blocks) are completely decoupled from each other and can be solved in parallel.

In the case of the preconditioned HMC algorithm, a partial decoupling of the fields on the blocks can be achieved by restricting the molecular dynamics evolution to a subset of all link variables, referred to as the *active link variables*, while keeping all

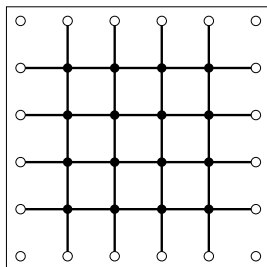


Fig. 2. Two-dimensional view of a 6^4 block showing the links on which the active link variables reside. Such links must have both endpoints in the same block and at most one endpoint on the interior boundary of the block (open circles).

other field variables fixed (see fig. 2). At the beginning or the end of every update cycle, the gauge field should then be translated by a random vector v ,

$$U(x, \mu) \rightarrow U(x + v, \mu) \quad \text{for all } x, \mu, \quad (3.9)$$

to ensure that all link variables are treated equally on average. Evidently, the same can also be achieved using several block coverings of the lattice alternately, but this tends to be rather more complicated from the programming point of view.

A moment of thought now reveals that the active link variables in different blocks are decoupled from each other if the last term in the hamiltonian (2.5) (the one involving the operator R_2) is neglected. The inner integrator $\mathfrak{J}_1(\epsilon_2, N_0, N_1)$ therefore factorizes into a product of integrators, one for each block, which evolve the active link variables residing there as if QCD would be reduced to that block. In particular, these parts of the integration can be carried out in parallel.

More important perhaps is the fact that the restriction to the active link variables leads to a reduction of the magnitude of the quark force that derives from the last term in the hamiltonian. This effect was anticipated in ref. [19] and will be discussed again in subsect. 4.2.

3.4 Update cycle

The generation of the next gauge-field configuration U' from the current configuration U thus proceeds in the following steps:

- (a) First the initial momenta $\Pi(x, \mu)$ and the pseudo-fermion fields $\phi_1(x)$ and $\phi_2(x)$ must be generated, with conditional probability proportional to e^{-H} . It suffices to generate the momenta of the active link variables, since only these will be updated.

The field ϕ_1 breaks up into block fields,

$$\phi_1 = \sum_{\text{all } \Lambda} \phi_\Lambda, \quad \phi_\Lambda = \hat{D}_\Lambda \eta_\Lambda, \quad (3.10)$$

where η_Λ is a gaussian random field supported on the even sites of block Λ , and the field ϕ_2 is similarly given in terms of a gaussian random field η_2 through

$$\phi_2 = R_2 \eta_2. \quad (3.11)$$

Both ϕ_2 and η_2 are in the linear space $V_{\partial\Omega^*}$ of boundary fields (appendix B).

(b) The molecular dynamics equations for the active link variables and their momenta must now be integrated from time 0 to time τ , the trajectory length. In the studies reported in this paper, the integration was performed by applying the integrator $\mathcal{J}_2(\tau, N_0, N_1, N_2)$ with some fixed step numbers N_0, N_1, N_2 . The computation of the forces F_0 and F_1 , which is required in this process, is entirely standard, while in the case of the force F_2 the key point to note is that

$$R_2^{-1} = 1 - P_{\partial\Omega^*} D^{-1} D_{\partial\Omega^*}. \quad (3.12)$$

In particular, for all variations ω of the active link variables,

$$(\omega, F_2) = 2\text{Re} \left(R_2^{-1} \phi_2, P_{\partial\Omega^*} D^{-1} \delta_\omega D D^{-1} D_{\partial\Omega^*} \phi_2 \right), \quad (3.13)$$

and the calculation of the force thus amounts to solving the Wilson–Dirac equation on the full lattice for two source fields. As already mentioned in sect. 2, any suitable preconditioner and solver can be used at this point. Here the Schwarz-preconditioned GCR solver described in ref. [20] was employed, with its own block grid chosen so as to minimize the average execution time.

(c) Once the molecular dynamics equations are integrated, the final configuration is accepted as the next one with probability

$$P_{\text{acc}} = \min \{ 1, e^{-\Delta H} \}, \quad \Delta H = H' - H, \quad (3.14)$$

where H and H' are the values of the hamiltonian of the initial and the final configuration respectively. Otherwise, i.e. if the proposed configuration is rejected, the old configuration is taken to be the next one. In both cases the selected configuration is translated by a random vector v , as discussed above, where v should be chosen with some care (see appendix C).

3.5 Choice of the block sizes

In principle any division of the lattice into non-overlapping blocks is acceptable, but the algorithm tends to become inefficient if the blocks are only a few lattice spacings wide, because in this case only a small fraction of the link variables get updated in each cycle. When the lattice is divided into 6^4 blocks, for example, the active link variables are a minority of 25%, and this percentage rises only slowly with the block size, reaching values greater than 50% when 12^4 and larger blocks are used.

Block sizes larger than 1 fm or so should also be avoided, however, because the Dirichlet boundary conditions then no longer provide a safe infrared cutoff on the spectrum of the block operators \hat{D}_Λ . The intended separation of the high and low modes of the Wilson–Dirac operator through the preconditioning is thus compromised and the algorithm slows down since the computation of the force F_1 becomes relatively time-consuming.

To sum up, the block sizes should be less than 1 fm, but as large as possible within this limit so as to maximize the fraction of the active link variables.

4. Tests of the algorithm

All simulations reported in this section were carried out on 8 nodes (16 processors) of a recent PC cluster, the same as the one described in appendix B of ref. [20]. The general programming strategies discussed in that paper were adopted here too and some further implementation details are given in appendix D.

4.1 Run parameters

Extensive simulations of two-flavour lattice QCD with the gauge and quark actions chosen here were previously performed by the SESAM and the T χ L collaborations [1–4] and, more recently, in the framework of the GRAL project [5,6] using the even–odd preconditioned HMC algorithm or the plain HMC algorithm with an ll-SSOR preconditioner [28] for the solver. Since most results of these studies were obtained at coupling $\beta = 6/g_0^2 = 5.6$, it was decided to carry out the tests of the Schwarz-preconditioned algorithm at this value of the coupling. Two lattices and three values of the hopping parameter $\kappa = (8 + 2m_0)^{-1}$ were considered, the one corresponding to the smallest quark mass being a new point (see table 1; for notational convenience the three runs at the smallest mass on the 32×24^3 lattice are distinguished by an upper index on κ).

Table 1. Simulation parameters

Lattice	Block size	κ	N_0, N_1, N_2	N_{tr}	P_{acc}
32×16^3	8^4	0.15750	4, 5, 4	8000	0.81
		0.15800	4, 5, 5	9100	0.86
		0.15825	4, 5, 6	9400	0.90
32×24^3	$8 \times 6^2 \times 12$	0.15750	4, 5, 5	4000	0.82
		0.15800	4, 5, 6	3950	0.80
		0.15825 ^a	4, 5, 7	800	0.71
		0.15825 ^b	4, 5, 8	2300	0.78
		0.15825 ^c	4, 5, 10	1100	0.87

In physical units the lattice spacings on these lattices decrease monotonically with the quark mass from 0.085 fm to about 0.078 fm [3] if the Sommer radius $r_0 = 0.5$ fm [29] is used as the basic reference scale[†]. The bare current-quark masses are then approximately 63, 35 and 21 MeV (see subsect. 4.6). Cutoff effects can still be fairly large at these lattice spacings, and a more meaningful statement about the quark masses would evidently have to include the appropriate renormalization factors, but these figures nevertheless provide a rough characterization of the physical situation at the simulation points.

Following ref. [1] the trajectory length τ was set to 0.5 in all cases. The mean distance in group space covered by the active link variables in the course of a trajectory is then fairly large already (about a third of the maximal distance). Initial runs of a few thousand trajectories were made on all lattices to ensure a safe thermalization, and N_{tr} trajectories were generated thereafter, as quoted in table 1.

4.2 Magnitude of the forces F_k

To a first approximation it seems reasonable to fix the step numbers N_0, N_1, N_2 in such a way that the increments $\epsilon_0 F_0, \epsilon_1 F_1, \epsilon_2 F_2$ are roughly of the same size. The magnitude of the forces was determined in the test runs, and the results of these calculations on the smaller lattices are shown in fig. 3. For the norm of an element

[†] If the mass of the ρ meson was used instead, slightly larger values would be obtained. However, since the ρ meson is a resonance and since its mass depends quite strongly on the quark mass, this way of setting the scale tends to be somewhat ambiguous in full QCD and subject to potentially large finite-size effects.

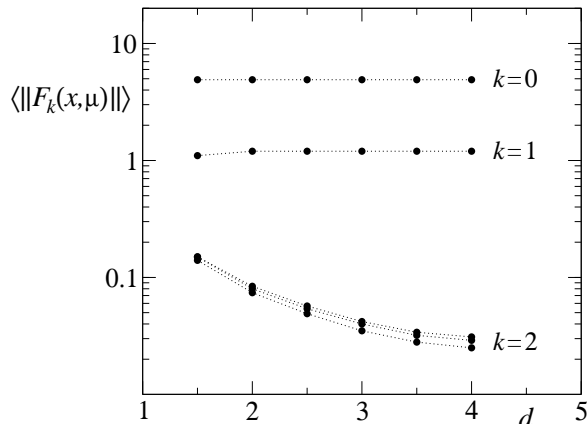


Fig. 3. Average magnitude of the forces F_k at the end of the molecular dynamics trajectories on the 32×16^3 lattice at distance d from the block boundary. Dotted lines are drawn to guide the eyes, and the three curves for F_2 correspond to the different quark masses (the mass dependence of the other curves is negligible).

X of the Lie algebra of $SU(3)$, the convention $\|X\|^2 = -2\text{tr}\{X^2\}$ was adopted here, and an average was taken over all gauge configurations and all links at the specified distance from the block boundary.

The magnitudes of the forces are thus strongly ordered, approximately like 32 : 8 : 1, and $\|F_2\|$ decreases rapidly as one moves towards the centre of the block. Moreover, a significant mass dependence is only seen in this force and only at the links where it is already very small. This behaviour can be understood by noting that the expression on the right of eq. (3.13) involves two quark propagators from the boundaries $\partial\Omega^*$ and $\partial\Omega$ to the link where the force is evaluated. The decay of the force away from the block boundary is then essentially a consequence of the corresponding property of the propagators.

Figure 3 suggests to set $N_0 = 4$, $N_1 = 8$ and to adjust N_2 so that a good acceptance rate is achieved. Some experimenting showed, however, that $N_1 = 5$ appears to be a better choice on the lattices that were simulated. For the values of N_2 quoted in table 1, the step size ϵ_2 was then in the range 0.05 – 0.13 and the average magnitude of the increments $\epsilon_k F_k$ was less than 0.031 in all cases.

4.3 Residues & reversibility

The computation of the quark forces F_1 and F_2 requires the solution of the Wilson–Dirac equation on the blocks Λ and on the full lattice, for two source fields in each case. On the full lattice, the Schwarz-preconditioned GCR solver [20] was applied

two times to the Wilson–Dirac equation directly, while on each block Λ the solutions were obtained simultaneously by solving the normal equation

$$A\psi = \eta, \quad A \equiv \hat{D}_\Lambda(\hat{D}_\Lambda)^\dagger, \quad (4.1)$$

using the conjugate-gradient (CG) algorithm. In this case the algorithm was stopped when the approximate solution ψ satisfied

$$\|\eta - A\psi\| \leq r_1\|\eta\| \quad (4.2)$$

for some specified tolerance r_1 . The analogous stopping criterion was applied, with tolerance r_2 , when the equation on the full lattice was solved.

At the beginning and the end of the molecular dynamics trajectories, the Wilson–Dirac equation must be solved a few more times, both on the blocks and on the full lattice, with tolerances \tilde{r}_1 and \tilde{r}_2 respectively. The BiCGstab algorithm [30,31] was used here to solve the block equations, since the solution is required for one source field only so that the application of the CG algorithm would be wasteful.

The tolerances chosen in the test runs,

$$r_1, r_2, \tilde{r}_1, \tilde{r}_2 = \begin{cases} 10^{-7}, 10^{-6}, 10^{-10}, 10^{-9} & \text{on the } 32 \times 16^3 \text{ lattices,} \\ 10^{-8}, 10^{-7}, 10^{-11}, 10^{-10} & \text{on the } 32 \times 24^3 \text{ lattices,} \end{cases} \quad (4.3)$$

are sufficiently small to guarantee the reversibility of the molecular dynamics trajectories to high precision. The maximal absolute deviation of the components of the link variables, for example, which was ever observed after a return trajectory was only 7×10^{-9} on the smaller and 7×10^{-10} on the larger lattices, while in the case of the hamiltonian the differences were less than 3×10^{-5} and 5×10^{-6} , respectively.

4.4 Stability

It is well known that instabilities in the numerical integration of the molecular dynamics equations may occur at small quark masses, which lead to violent fluctuations in ΔH and to a stagnation of the algorithm in extreme cases. Choosing smaller integration step sizes usually cures the problem, but also increases the computer time required per trajectory (see refs. [8,11] for example).

In the tests of the Schwarz-preconditioned algorithm, severe integration instabilities were only rarely seen in spite of the fact that the step size ϵ_2 was set to relatively large values. A small algorithmic modification, referred to as the *replay trick* [32], was nevertheless included in order to safely avoid periods of stagnation. Essentially

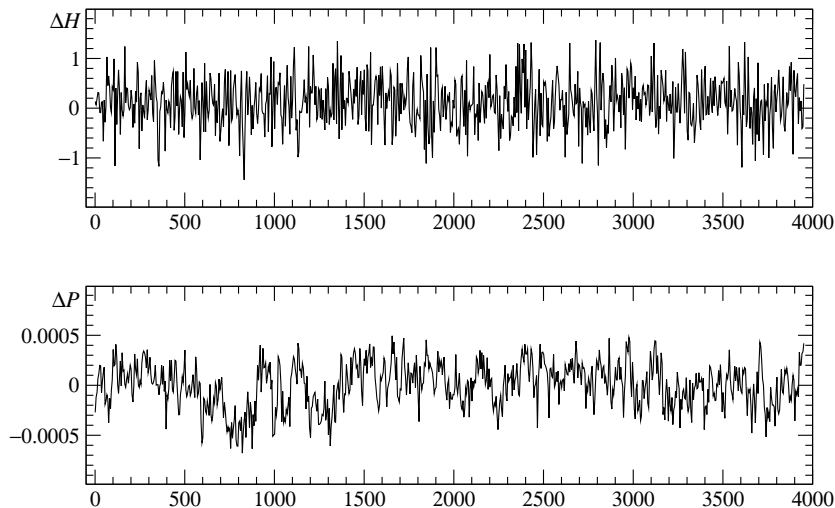


Fig. 4. Histories of ΔH and of the deviation ΔP of the average plaquette from its mean value at $\kappa = 0.15800$ on the 32×24^3 lattice as a function of the trajectory number. Only the values after every 5th trajectory are plotted.

the modification amounts to replaying the trajectories with values of $|\Delta H|$ above a specified threshold, using a smaller step size and a somewhat complicated acceptance rule that preserves detailed balance.

For illustration, a typical time series of ΔH (after including the replay trick) is shown in fig. 4. The replay threshold was set to 1.5 in this case and the overhead in computer time that was caused by the trajectory replays was about 2%. Also shown in the figure are the fluctuations of the average plaquette

$$P = \frac{1}{3N_p} \sum_p \text{Re tr}\{U_p\}, \quad (4.4)$$

where the sum runs over all N_p plaquettes on the lattice and U_p denotes the ordered product of the link variables around the plaquette p . As will be discussed shortly, these fluctuations are quite correlated, but otherwise do not seem to have any special features. In particular, the associated histogram has a nearly gaussian shape.

The fact that the (massive) Wilson–Dirac operator is not protected from having arbitrarily small eigenvalues was always a source of concern and may well be the cause for the integration instabilities [11]. An interesting quantity to consider in this connection is the average number $\langle N_{\text{GCR}} \rangle$ of Schwarz-preconditioned GCR iterations that are required for the solution of the Wilson–Dirac equation on the full lattice along a given trajectory. While catastrophically large iteration numbers were never

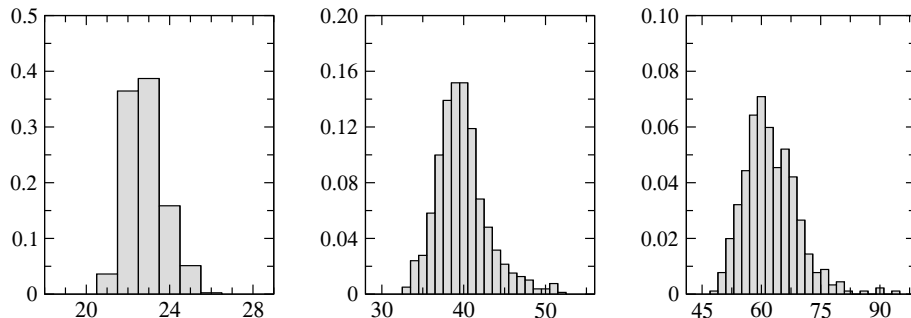


Fig. 5. Probability distribution of the average iteration number $\langle N_{\text{GCR}} \rangle$ per application of the Schwarz-preconditioned GCR solver along a given trajectory. From left to right the results obtained on the 32×24^3 lattice at $\kappa = 0.15750, 0.15800, 0.15825^b$ are shown.

observed, the distributions shown in fig. 5 have a tail that extends to fairly high values of $\langle N_{\text{GCR}} \rangle$ at the smallest quark mass. The replay overhead on the 32×24^3 lattice was actually as large as 20–30% at this mass, except in the last run where the replay threshold was set to 3.0 and no trajectories were replayed.

4.5 Autocorrelation times

An estimation of the relevant autocorrelation times is clearly essential in the present context, since the efficiency of the algorithm can only be determined when these are known. Unfortunately the available statistics is insufficient for a solid “error of the error” analysis [33], and the values for the integrated autocorrelation times quoted below should therefore be taken as first estimates only.

The autocorrelation functions of the average plaquette P and the average number $\langle N_{\text{GCR}} \rangle$ of GCR iterations are plotted in fig. 6. An approximation to the four-point autocorrelation function introduced by Madras and Sokal [34] was used here to determine the statistical errors (see appendix E). As usual the associated integrated autocorrelation times are obtained by summing the autocorrelation functions up to some maximal time lag, referred to as the summation window. The particular prescription adopted here was to truncate the sums at the first point where the autocorrelation function vanishes within errors. In general this rule yields consistent results and summation windows a few times larger than the calculated autocorrelation times.

The values of the integrated autocorrelation times listed in table 2 seem to be quite a bit higher than those obtained in previous studies of two-flavour QCD, but the comparison is not straightforward and must in any case remain uncertain to some

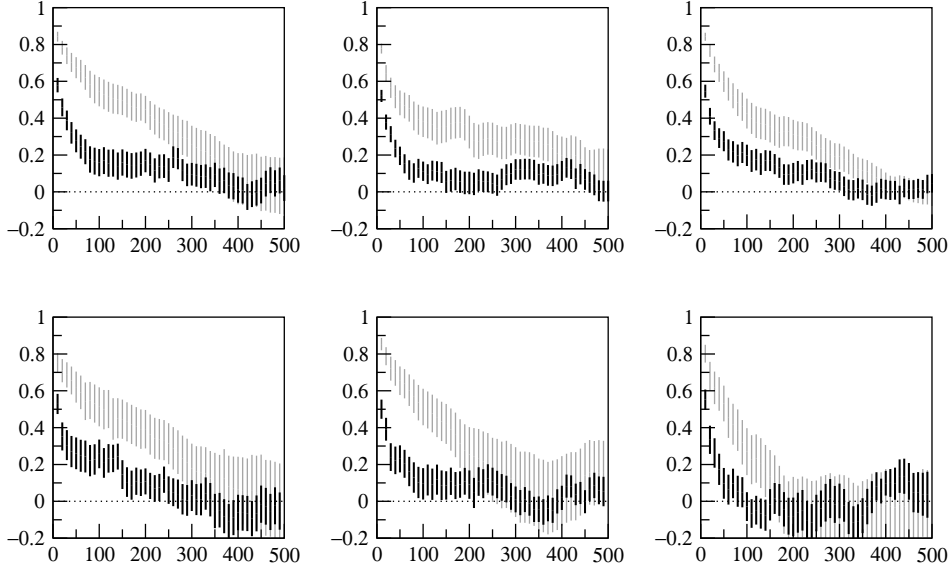


Fig. 6. Normalized autocorrelation functions of the average plaquette P (dark error band) and the average number $\langle N_{\text{GCR}} \rangle$ of GCR iterations (grey band). In the first and the second row of plots the lattice size is 32×16^3 and 32×24^3 respectively, and the hopping parameters increase from left to right as in fig. 5.

extent in view of the large statistical errors (see subsect. 4.7). It should also be noted that the solver iteration numbers are usually a worst case, and more physical quantities (hadron masses in particular) typically have much smaller integrated autocorrelation times.

Whether there is a systematic trend in the autocorrelation times as a function of the quark mass or the lattice size is difficult to tell from the figures listed in table 2. There is, however, no indication that the autocorrelation times grow when the quark mass is lowered. Some of the runs were perhaps a bit too short to safely exclude biased results, and longer simulations may be required to firmly establish the decrease of the autocorrelation times as a function of the step size ϵ_2 suggested by the last three entries in the table.

4.6 Quark and pion masses

In this algorithmic study, the computation of the current-quark mass and the pion mass is not of central interest, but it helps to determine the physical situation on the simulated lattices, as discussed at the beginning of this section.

Since a very accurate determination of the masses is not required, error reduction

Table 2. Integrated autocorrelation times *

Lattice	κ	$\tau_{\text{int}}[P]$	$\tau_{\text{int}}[\langle N_{\text{GCR}} \rangle]$
32×16^3	0.15750	68(25)	168(42)
	0.15800	32(7)	162(56)
	0.15825	57(18)	135(39)
32×24^3	0.15750	53(22)	144(51)
	0.15800	33(11)	122(36)
	0.15825 ^a	33(13)	84(24)
	0.15825 ^b	19(5)	65(20)
	0.15825 ^c	12(4)	22(6)

* In numbers of trajectories of length $\tau = 0.5$

techniques were not applied and the masses were obtained straightforwardly from the two-point functions of the isospin axial current and density. In terms of the quark field ψ and the antiquark field $\bar{\psi}$, the latter are given by

$$A_\mu^a = \bar{\psi} \gamma_\mu \gamma_5 \frac{1}{2} \tau^a \psi, \quad P^a = \bar{\psi} \gamma_5 \frac{1}{2} \tau^a \psi, \quad (4.5)$$

where τ^1, τ^2, τ^3 denote the isospin Pauli matrices. As usual the two-point functions were evaluated at vanishing spatial momentum,

$$\sum_{x_1, x_2, x_3} \langle P^a(x) P^b(0) \rangle \equiv \frac{1}{2} \delta^{ab} f_{\text{PP}}(x_0), \quad (4.6)$$

$$\sum_{x_1, x_2, x_3} \langle A_0^a(x) P^b(0) \rangle \equiv \frac{1}{2} \delta^{ab} f_{\text{AP}}(x_0), \quad (4.7)$$

and the appropriate signed average of the calculated functions at time x_0 and $T - x_0$ was taken.

In the test runs, the gauge-field configurations generated after every 100 update cycles were saved to disk, allowing physical quantities such as the quark and the pion mass to be calculated later. The fields in these ensembles are only weakly correlated, and no systematic increase in the naive statistical errors was in fact observed when the measured values of the two-point functions $f_{\text{PP}}(x_0)$ and $f_{\text{AP}}(x_0)$ were averaged over small bins of successive configurations. For the mass calculations the values of the two-point functions were therefore assumed to be statistically independent and

Table 3. Average plaquette, current-quark mass and pion mass

Lattice	κ	P	am	am_π
32×16^3	0.15750	0.57255(6)	0.0279(4)	0.298(5)
	0.15800	0.57335(4)	0.0153(4)	0.242(4)
	0.15825	0.57387(5)	0.0092(4)	0.209(7)
32×24^3	0.15750	0.57250(4)	0.0273(4)	0.280(3)
	0.15800	0.57344(3)	0.0143(3)	0.188(5)
	0.15825 ^{all}	0.57383(2)	0.0084(4)	0.153(4)

the results were checked by repeating the calculations with the data averaged over bins of 2 or 3 measurements.

The conservation of the axial current in the continuum limit implies that the ratio

$$\{f_{\text{AP}}(x_0 + 1) - f_{\text{AP}}(x_0 - 1)\}\{4f_{\text{PP}}(x_0)\}^{-1} \quad (4.8)$$

is independent of x_0 and equal to the bare current-quark mass m , up to terms that vanish proportionally to the lattice spacing. In the range $8 \leq x_0 \leq 16$ the data for the ratio were actually found to be constant within errors. The quark mass was then extracted through a correlated least-squares fit of the ratio in this range, using jackknife error estimates for the covariance matrix.

The pion mass m_π was calculated in the same way by fitting the effective mass $m_{\text{eff}}(x_0)$ at large times x_0 . At any given x_0 , the effective mass is obtained by solving the equation

$$\frac{h(x_0 - 1)}{h(x_0)} = \frac{f_{\text{PP}}(x_0 - 1)}{f_{\text{PP}}(x_0)}, \quad h(x_0) \equiv e^{-x_0 M} + e^{-(T-x_0)M}, \quad (4.9)$$

for M and setting $m_{\text{eff}}(x_0) = M$. The associated covariance matrix was again calculated using jackknife bins and the fit ranges were chosen so that a good fit quality was obtained.

Where a comparison is possible, the results listed in table 3 coincide with those published by the SESAM, T χ L and GRAL collaborations [1–6] within 1 or 2 sigma, an exception being a deviation by 3 sigma of the pion mass at $\kappa = 0.15750$ on the 32×16^3 lattice. The quark masses change only slightly with the lattice size, as it should be close to the continuum limit, while the size-dependence of the pion mass

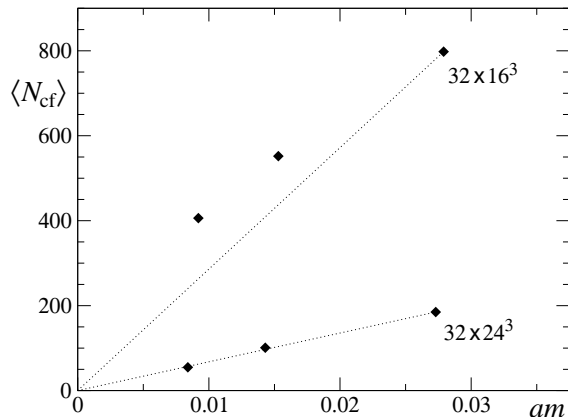


Fig. 7. Average number $\langle N_{\text{cf}} \rangle$ of accepted gauge-field configurations generated per day by the Schwarz-preconditioned HMC algorithm on 8 nodes of a recent PC cluster (described in ref. [20], appendix B), as a function of the bare current-quark mass. The point at the smallest mass on the 32×24^3 lattice is from the last run in table 1 and the linear scaling curves (dotted lines) are drawn for comparison with the data.

is not small on these lattices [5,6]. In physical units the quark and the pion masses quoted on the last line of table 3 are about 21 MeV and 386 MeV respectively (if the scale is set through the Sommer radius).

4.7 Speed and efficiency of the algorithm

In practice the average number of accepted gauge-field configurations generated per day on the computer that is used for the simulations is a relevant performance figure. As can be seen from fig. 7, the experience made with the Schwarz-preconditioned HMC is quite encouraging in this respect, given the fact that the tests were performed on a relatively small machine. In the most time-critical parts of the program, the machine delivered about 26 Gflop/s [20], and the total computer time spent for the tests was a little more than half a year.

At the smallest quark mass that was considered, most of the time is used for the solution of the Wilson–Dirac equation on the full lattice. The situation is different at the larger quark masses, where the solver converges faster while the time spent in the other parts of the program is nearly unchanged. For this reason, and since the step number N_2 had to be adjusted slightly, the configuration production rate does not follow a simple scaling law with respect to the quark mass. In particular, the three lower points in fig. 7 are only accidentally fitted by the dotted line.

An interesting measure for the efficiency of the Schwarz-preconditioned algorithm

Table 4. Values of the cost figure ν

Lattice	κ	ν
32×16^3	0.15750	0.75(28)
	0.15800	0.42(9)
	0.15825	0.86(27)
32×24^3	0.15750	0.69(29)
	0.15800	0.50(17)
	0.15825 ^a	0.56(22)
	0.15825 ^b	0.36(10)
	0.15825 ^c	0.28(9)

is provided by the cost figure

$$\nu = 10^{-3} (2N_2 + 3) \tau_{\text{int}}[P]. \quad (4.10)$$

On average, this is the number of times the Wilson–Dirac equation must be solved on the full lattice, in units of thousands, before a statistically independent value of the average plaquette P is obtained. Evidently ν is independent of the machine, the program and the particular solver which are used. The numbers listed in table 4 show that the algorithm is remarkably stable in these terms, and there certainly is no indication, in the parameter range considered and within the errors quoted, that it would slow down towards smaller quark masses or larger lattices.

If another or no preconditioner is used for the HMC algorithm, the cost figure ν may be defined in the same way, with N_2 replaced by the appropriate step number. In refs. [1–6], for example, the plain HMC algorithm was studied at the same gauge coupling and hopping parameters $\kappa = 0.15750$ and $\kappa = 0.15800$ which were considered here. On the 32×16^3 lattice the corresponding values of ν , as calculated from the run parameters and autocorrelation times quoted in ref. [6], are equal to 1.0(6) and 2.8(8) respectively. These numbers rise to 1.8(8) and 5.1(5) on the 40×24^3 lattice, which shows quite clearly that the efficiency of the plain HMC algorithm decreases when the lattice size is increased or if the quark mass is taken to smaller values. In particular, already at $\kappa = 0.15800$ (where the pion mass is approximately 465 MeV) the Schwarz-preconditioned algorithm is much more efficient.

Although different lattice formulations were chosen in most cases, it is interesting to note that large values of ν are common to all previous simulations of two-flavour

QCD at small quark masses. In a study conducted by the UKQCD collaboration [8], for example, using the even–odd preconditioned HMC algorithm, the cost figure on a 32×16^3 lattice at $m_\pi \simeq 420$ MeV was 5.5(11). Significantly smaller masses were reached by the CP-PACS collaboration on a coarse 24×12^3 lattice [11], and in these simulations ν ranged from 9.4(18) at $m_\pi \simeq 398$ MeV to 29(10) at $m_\pi \simeq 255$ MeV.

5. Concluding remarks

The Schwarz-preconditioned HMC algorithm is intended for simulations of lattice QCD at small lattice spacings and small quark masses. It is particularly well suited for parallel processing, which can be a decisive advantage when the continuum limit is approached and very large lattices have to be simulated. Many of the theoretically expected properties of the algorithm were confirmed in the tests reported in this paper, and although important uncertainties remain, there are clear indications that the algorithm does indeed have a favourable scaling behaviour with respect to the quark mass.

So far only the standard Wilson formulation of lattice QCD was considered, but $O(a)$ improvement and double-plaquette terms can be easily included in the Schwarz-preconditioned algorithm. Whether its excellent scaling properties will be preserved is difficult to foresee, however, because the autocorrelation times are unpredictable. Independently of the lattice formulation, the algorithm is not expected to perform particularly well at large quark masses or at lattice spacings larger than 0.1 fm or so. The problem on coarse lattices simply is that all choices of the block sizes tend to be inappropriate from one or the other point of view (cf. subsect. 3.5).

The particular Schwarz preconditioner that was considered here is only one example of a domain decomposition preconditioner. Close to the continuum limit more complicated preconditioners, based on a hierarchy of block grids perhaps or alternative domain decompositions, may conceivably be more efficient. The potential for further accelerations along these lines is limited, however, until significantly larger step numbers are required than those quoted in table 1.

I am indebted to Rainer Sommer for many helpful discussions on QCD simulation algorithms and to Ulli Wolff for correspondence on the analysis of simulation time series. Thanks also go to Boris Orth for sending a copy of his PhD thesis prior to publication, and to him and Thomas Lippert for correspondence on the SESAM, T χ L and GRAL projects. The simulations reported in this paper were carried out

on a PC cluster at the Institut für Theoretische Physik der Universität Bern, which was funded in part by the Schweizerischer Nationalfonds. I thank both institutions for the continuous support given to this project.

Appendix A. SU(3) exponential function

In the course of the numerical integration of the molecular dynamics equations, the link variables are updated by left-multiplication with a matrix function $E(X)$, where X is proportional to the field momentum at the given link. $E(X)$ is usually taken to be the exponential function in SU(3), but there are alternative choices that are theoretically equally acceptable and easier to implement.

To ensure that the leap-frog integration will be well-defined, reversible and quadratically convergent, the following properties must hold:

- (1) $E(X)$ is a smooth mapping from the Lie algebra of SU(3) to the group.
- (2) The function satisfies $E(X)E(-X) = 1$ for all X .
- (3) At small t the asymptotic expansion $E(tX) = 1 + tX + \frac{1}{2}t^2X^2 + O(t^3)$ holds.

All these requirements can be met by setting

$$E(X) = U_1U_2U_3U_2U_1, \tag{A.1}$$

where U_1 , U_2 and U_3 are certain SU(2) rotations in the (12), (13) and (23) subspaces respectively. They are obtained by representing the anti-hermitian traceless matrix X as a sum of the three matrices

$$Y_1 = \begin{pmatrix} x_1 & X_{12} & 0 \\ X_{21} & -x_1 & 0 \\ 0 & 0 & 0 \end{pmatrix}, \quad x_1 = \frac{1}{3}(X_{11} - X_{22}), \tag{A.2}$$

$$Y_2 = \begin{pmatrix} x_2 & 0 & X_{13} \\ 0 & 0 & 0 \\ X_{31} & 0 & -x_2 \end{pmatrix}, \quad x_2 = \frac{1}{3}(X_{11} - X_{33}), \tag{A.3}$$

$$Y_3 = \begin{pmatrix} 0 & 0 & 0 \\ 0 & x_3 & X_{23} \\ 0 & X_{32} & -x_3 \end{pmatrix}, \quad x_3 = \frac{1}{3}(X_{22} - X_{33}). \tag{A.4}$$

Evidently, these are generators of the $SU(2)$ subgroups just mentioned, and it is then straightforward to prove that

$$U_1 = \left(1 + \frac{1}{4}Y_1\right) \left(1 - \frac{1}{4}Y_1\right)^{-1}, \quad (\text{A.5})$$

$$U_2 = \left(1 + \frac{1}{4}Y_2\right) \left(1 - \frac{1}{4}Y_2\right)^{-1}, \quad (\text{A.6})$$

$$U_3 = \left(1 + \frac{1}{2}Y_3\right) \left(1 - \frac{1}{2}Y_3\right)^{-1} \quad (\text{A.7})$$

is a possible choice of the matrices U_k . The inversions in these equations can be worked out analytically and are numerically safe, since the Y_k 's have purely imaginary eigenvalues. In particular, it is straightforward to write a fast program that computes $E(X)$ for any given X practically to machine precision.

Appendix B. Boundary fields

In this appendix the space $V_{\partial\Omega^*}$ of boundary fields is specified explicitly. The choice of this space is actually not unique, but it should be such that the associated orthonormal projector $P_{\partial\Omega^*}$ satisfies

$$D_{\partial\Omega^*} P_{\partial\Omega^*} = D_{\partial\Omega^*}. \quad (\text{B.1})$$

This property guarantees that the determinant of the Schur complement in eq. (3.5) coincides with the determinant of the projected operator R_2 , which is all what is assumed in sects. 3 and 4.

The action of the operator $D_{\partial\Omega^*}$ on an arbitrary quark field $\psi(x)$ is given by

$$D_{\partial\Omega^*} \psi(x) = -\theta_{\Omega^*}(x) \sum_{\mu=0}^3 \left\{ \frac{1}{2} (1 - \gamma_\mu) \theta_\Omega(x + \hat{\mu}) U(x, \mu) \psi(x + \hat{\mu}) + \frac{1}{2} (1 + \gamma_\mu) \theta_\Omega(x - \hat{\mu}) U(x - \hat{\mu}, \mu)^{-1} \psi(x - \hat{\mu}) \right\}, \quad (\text{B.2})$$

where $\theta_\Omega(x)$ and $\theta_{\Omega^*}(x)$ are the characteristic functions of Ω and Ω^* . As illustrated by fig. 8, the terms on the right-hand side of this equation move the Dirac spinors from $\partial\Omega^*$ to $\partial\Omega$ and multiply them with the projectors $\frac{1}{2}(1 \pm \gamma_\mu)$ and the appropriate

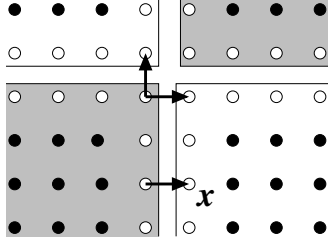


Fig. 8. The hopping terms in $D_{\partial\Omega^*}$ move the quark spinors from the interior to the exterior boundary points of the black blocks. Depending on the position of the inner point, the spinor is moved in one or more directions.

link variables. In particular, two components of the spinors residing on the subset

$$[\partial\Omega^*] = \{x \in \partial\Omega^* \mid x + \hat{\mu} \in \partial\Omega \text{ or } x - \hat{\mu} \in \partial\Omega \text{ for one value of } \mu \text{ only}\} \quad (\text{B.3})$$

are lost irretrievably through the application of the projectors.

It is now straightforward to show that the operator

$$P_{\partial\Omega^*} \psi(x) = \begin{cases} 0 & \text{if } x \notin \partial\Omega^*, \\ \frac{1}{2}(1 + \gamma_\mu)\psi(x) & \text{if } x \in [\partial\Omega^*] \text{ and } x + \hat{\mu} \in \partial\Omega, \\ \frac{1}{2}(1 - \gamma_\mu)\psi(x) & \text{if } x \in [\partial\Omega^*] \text{ and } x - \hat{\mu} \in \partial\Omega, \\ \psi(x) & \text{otherwise,} \end{cases} \quad (\text{B.4})$$

satisfies eq. (B.1). Moreover, this choice excludes the trivial nullspace of $D_{\partial\Omega^*}$ and thus minimizes the dimension of the space $V_{\partial\Omega^*}$ of boundary quark fields.

Appendix C. Translation vectors

The field translations at the end of the update cycles of the Schwarz-preconditioned algorithm should ideally be such that all link variables are visited at approximately the same rate. In particular, long gaps between subsequent updates of a given link variable should be avoided as far as possible. One might think that a purely random choice of the translation vectors v will be acceptable from this point of view, but the visiting frequency on some links can actually be far below average in this case, even after hundreds of update cycles.

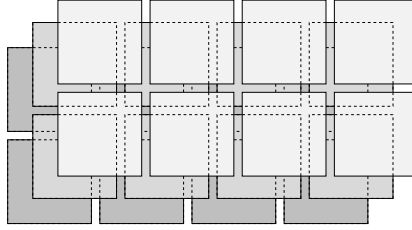


Fig. 9. Three copies of a block grid in two dimensions, two of them being translated along a diagonal direction at regular distances. Taking the boundary conditions into account, the lattice is completely covered by the blocks in these grids.

More balanced visiting frequencies can be obtained by adopting a quasi-random scheme, where a purely random choice of v is followed, in the next few update cycles, by translations along a diagonal lattice direction in regular steps (see fig. 9). If the lattice is divided into blocks of size 8^4 , for example, performing a random translation and then three times a translation by the vector

$$v = (2, 2, 2, 2) \tag{C.1}$$

yields a fairly narrow visiting distribution. For general block sizes b_μ , it suffices to take $n - 1$ regular steps by the vector

$$v = (b_0, b_1, b_2, b_3)/n \tag{C.2}$$

(or close-by integer vectors), where $n = \frac{1}{2} \min\{10, b_0, b_1, b_2, b_3\}$.

Appendix D. Programming issues

The programming of the Schwarz-preconditioned algorithm is not completely trivial, particularly so on parallel computers, where the block decomposition of the lattice gives rise to additional complications. Object orientation and generic programming are useful general strategies that may be applied here [20], and some more specific issues will now be addressed.

D.1 Parallelization

Clearly the communication overhead is minimized if each block in the domains Ω and Ω^* is fully contained in one of the sublattices on which the processors of a parallel

computer operate. This was the case in the test runs reported here, but more flexible assignments may eventually be needed, where the processor sublattices divide the blocks in some way.

On machines with symmetric multiprocessing nodes, for example, the natural choice is to contain the blocks in the node sublattices. In this case the processors can operate on the block fields in a shared-memory mode and the network is only used when the global fields get involved. In general the communication overhead can always be reduced by dividing the blocks into smaller blocks that are fully contained in the processor sublattices. The Schwarz-preconditioned GCR solver may then be set up on this block grid and be used for the solution of the Wilson–Dirac equation on both the full lattice and the big blocks.

D.2 Block fields

In the program a block may be defined through a data structure that contains the relevant geometrical information (embedding and nearest-neighbour indices), the local gauge field and a set of quark fields. An obvious advantage of this approach is that the operations on these fields can proceed locally without having to gather and scatter any data from and to the global fields. With a proper layout of the local fields in memory, streaming data accesses, and hence a higher processing speed, are thus made possible.

Most computations are actually local operations, an exception being the calculation of the force F_2 , which requires the solution of the Wilson–Dirac equation on the full lattice. The current values of the gauge fields on the blocks may need to be copied to the global fields at this point, but this is a minor complication, since the fields must be copied only once per force calculation.

D.3 Single-precision acceleration

In the course of the numerical integration of the molecular dynamics equations, an exponential amplification of rounding errors is possible and important significance losses are in any case unavoidable when the difference ΔH is calculated at the end of the trajectories. The algorithm was therefore implemented using double-precision (64 bit) data and arithmetic for all fields.

Through the intermediate use of single-precision data and arithmetic, the CG and the Schwarz-preconditioned GCR solvers for the Wilson–Dirac equation can, however, be accelerated without compromising the precision of the final results [35,20]. On current PC processors, where the relevant single-precision programs are significantly faster than their double-precision versions, an acceleration by a factor 2 or so can be achieved in this way.

Appendix E. Calculation of autocorrelation times

In practice the calculation of autocorrelation times tends to be somewhat ambiguous unless the available time series are very long. The particular prescriptions that were used in this paper are described in the following for the case of a primary observable A such as the average plaquette. Essentially the discussion follows refs. [33,34] where further details and alternative strategies can be found.

E.1 Preliminaries

Let a_1, a_2, \dots, a_N be a time series of measurements of A obtained in the course of a numerical simulation. It is helpful to imagine that infinitely many such simulations were made, with independent random numbers so that the different runs may be assumed to be uncorrelated. The true expectation value of A is then

$$a = \langle a_i \rangle, \tag{E.1}$$

where $\langle \dots \rangle$ denotes the average over the infinite set of uncorrelated simulations. This value should be distinguished from the average

$$\bar{a} = \frac{1}{N} \sum_{i=1}^N a_i, \tag{E.2}$$

which is obtained in a particular simulation. From the point of view of the set of simulations, \bar{a} is a stochastic variable with expectation value $\langle \bar{a} \rangle = a$.

In terms of the true autocorrelation function

$$\Gamma(t) = \Gamma(-t) = \langle (a_i - a)(a_{i+t} - a) \rangle, \tag{E.3}$$

the statistical variance of the measured value \bar{a} of A is given by

$$\sigma^2 = \langle (\bar{a} - a)^2 \rangle = \frac{1}{N^2} \sum_{i,j=1}^N \Gamma(i-j). \tag{E.4}$$

At large N this equation may be written in the form

$$\sigma^2 = 2\tau_{\text{int}}\sigma_0^2 \tag{E.5}$$

where $\sigma_0^2 = \Gamma(0)/N$ is the naive variance and

$$\tau_{\text{int}} = \frac{1}{2} + \sum_{t=1}^{\infty} \frac{\Gamma(t)}{\Gamma(0)} \quad (\text{E.6})$$

the integrated autocorrelation time.

E.2 Madras–Sokal approximation

The expression

$$\bar{\Gamma}(t) = \frac{1}{N-t} \sum_{i=1}^{N-t} (a_i - \bar{a})(a_{i+t} - \bar{a}) \quad (\text{E.7})$$

provides an approximation to the true autocorrelation function, which can be computed from the available time series. Its expectation value coincides with $\Gamma(t)$ up to terms that are negligible (at large N) with respect to the deviation

$$\delta\Gamma(t) = \bar{\Gamma}(t) - \langle \bar{\Gamma}(t) \rangle, \quad (\text{E.8})$$

whose variance determines the statistical error of $\bar{\Gamma}(t)$.

The covariance of $\delta\Gamma(t)$ involves a sum over the four-point autocorrelation function, which is usually difficult to compute precisely from the available data alone. However, as first noted by Madras and Sokal [34], the disconnected parts of the four-point function make the dominant contribution to the sum, and if only these are kept, the covariance becomes

$$\langle \delta\Gamma(t)\delta\Gamma(s) \rangle \simeq \frac{1}{N} \sum_{k=-\infty}^{\infty} \{ \Gamma(k)\Gamma(k+t-s) + \Gamma(k+t)\Gamma(k-s) \}, \quad (\text{E.9})$$

where $t, s \ll N$ was assumed and any subleading terms were neglected. It is then also possible to derive the elegant formula

$$\langle \delta\rho(t)^2 \rangle \simeq \frac{1}{N} \sum_{k=1}^{\infty} \{ \rho(k+t) + \rho(k-t) - 2\rho(k)\rho(t) \}^2 \quad (\text{E.10})$$

for the variance of the normalized autocorrelation function $\rho(t) = \Gamma(t)/\Gamma(0)$.

E.3 Practical procedure

Equations (E.6) and (E.10) can be evaluated by substituting $\bar{\rho}(t) = \bar{\Gamma}(t)/\bar{\Gamma}(0)$ for the normalized autocorrelation function and truncating the sums at some sufficiently large time lag. In the case of the variance of the autocorrelation function,

$$\langle \delta\rho(t)^2 \rangle \simeq \frac{1}{N} \sum_{k=1}^{t+\Lambda} \{ \bar{\rho}(k+t) + \bar{\rho}(k-t) - 2\bar{\rho}(k)\bar{\rho}(t) \}^2, \quad (\text{E.11})$$

the choice of the cutoff Λ is not critical and values of $\Lambda \geq 100$ gave consistent results for all error bands plotted in fig. 6.

The integrated autocorrelation time may then be determined through the sum

$$\tau_{\text{int}} = \frac{1}{2} + \sum_{t=1}^W \bar{\rho}(t), \quad (\text{E.12})$$

in which the summation window W is set to the first time lag t where

$$\bar{\rho}(t) \leq \langle \delta\rho(t)^2 \rangle^{1/2}. \quad (\text{E.13})$$

Other criteria [33,34] could be applied at this point and may be preferable when the statistics allows for an optimization of the summation window. The Madras–Sokal formula

$$\langle \delta\tau_{\text{int}}^2 \rangle \simeq \frac{4W+2}{N} \tau_{\text{int}}^2 \quad (\text{E.14})$$

may finally be used to estimate the statistical error of the autocorrelation time.

References

- [1] Th. Lippert et al. (SESAM and T χ L collab.), Nucl. Phys. B (Proc. Suppl.) 60A (1998) 311
- [2] N. Eicker et al. (SESAM collab.), Phys. Rev. D59 (1999) 014509
- [3] G. S. Bali et al. (SESAM and T χ L collab.), Phys. Rev. D62 (2000) 054503
- [4] N. Eicker, Th. Lippert, B. Orth, K. Schilling, Nucl. Phys. B (Proc. Suppl.) 106 (2002) 209
- [5] B. Orth, Th. Lippert, K. Schilling, Nucl. Phys. B (Proc. Suppl.) 129 (2004) 173

- [6] B. Orth, Finite-size effects in lattice QCD with dynamical Wilson fermions, PhD thesis WUB-DIS 2004-03 (University of Wuppertal, Germany, 2004)
- [7] C. R. Allton et al. (UKQCD collab.), Phys. Rev. D60 (1999) 034507; *ibid.* D65 (2002) 054502
- [8] C. R. Allton et al. (UKQCD collab.), Phys. Rev. D70 (2004) 014501
- [9] A. Ali Khan et al. (CP-PACS collab.), Phys. Rev. Lett. 85 (2000) 4674 [E: *ibid.* 90 (2003) 029902]; Phys. Rev. D65 (2002) 054505 [E: *ibid.* D67 (2003) 059901]
- [10] S. Aoki et al. (JLQCD collab.) Phys. Rev. D68 (2003) 054502
- [11] Y. Namekawa et al. (CP-PACS collab.), Light hadron spectroscopy in two-flavor QCD with small sea quark masses, arXiv: hep-lat/0404014
- [12] Y. Saad, Iterative methods for sparse linear systems, 2nd ed. (SIAM, Philadelphia, 2003); see also <http://www-users.cs.umn.edu/~saad/>
- [13] S. Duane, A. D. Kennedy, B. J. Pendleton, D. Roweth, Phys. Lett. B195 (1987) 216
- [14] Ph. de Forcrand, T. Takaishi, Nucl. Phys. B (Proc. Suppl.) 53 (1997) 968
- [15] M. J. Peardon. Accelerating the Hybrid Monte Carlo algorithm with ILU preconditioning, arXiv: hep-lat/0011080
- [16] M. Hasenbusch, Phys. Lett. B519 (2001) 177
- [17] M. Hasenbusch, K. Jansen, Nucl. Phys. B659 (2003) 299
- [18] M. Della Morte et al. (ALPHA collab.), Comput. Phys. Commun. 156 (2003) 62
- [19] M. Lüscher, J. High Energy Phys. 0305 (2003) 052
- [20] M. Lüscher, Comput. Phys. Commun. 156 (2004) 209
- [21] K. G. Wilson, Phys. Rev. D10 (1974) 2445
- [22] B. Sheikholeslami, R. Wohlert, Nucl. Phys. B 259 (1985) 572
- [23] M. Lüscher, S. Sint, R. Sommer, P. Weisz, Nucl. Phys. B478 (1996) 365
- [24] Y. Iwasaki, Renormalization group analysis of lattice theories and improved lattice action. 2. Four-dimensional non-abelian $SU(N)$ gauge model, Tsukuba preprint UTHEP-118 (1983); Nucl. Phys. B258 (1985) 141
- [25] M. Lüscher, P. Weisz, Commun. Math. Phys. 97 (1985) 59 [E: *ibid.* 98 (1985) 433]; Phys. Lett. B158 (1985) 250
- [26] J. C. Sexton, D. H. Weingarten, Nucl. Phys. B380 (1992) 665
- [27] M. J. Peardon, J. C. Sexton (TrinLat Collab.), Nucl. Phys. B (Proc. Suppl.) 119 (2003) 985
- [28] S. Fischer et al., Comput. Phys. Commun. 98 (1996) 20; Nucl. Phys. B (Proc. Suppl.) 53 (1997) 990
- [29] R. Sommer, Nucl. Phys. B411 (1994) 839
- [30] H. A. van der Vorst, SIAM J. Sci. Stat. Comput. 13 (1992) 631

- [31] A. Frommer, V. Hannemann, B. Nöckel, T. Lippert, K. Schilling, *Int. J. Mod. Phys. C* 5 (1994) 1073
- [32] M. Lüscher, R. Sommer, in preparation
- [33] U. Wolff, *Comput. Phys. Commun.* 156 (2004) 143 [E: hep-lat/0306017 v3]
- [34] N. Madras, A. D. Sokal, *J. Stat. Phys.* 50 (1988) 109
- [35] L. Giusti, C. Hoelbling, M. Lüscher, H. Wittig, *Comput. Phys. Commun.* 153 (2003) 31